DET NATURVIDENSKABELIGE FAKULTET
KØBENHAVNS UNIVERSITET
Center for Quantum Devices

Bachelor's Thesis

Marina Hesselberg

Fabrication and Characterization of an InSb Quantum Well Device

Supervisor: Charles Marcus

Submitted: 01/10/13

Acknowledgements

"ONE LIFE / ONE PAIN"
I would like to express my gratitude to Charles Marcus for guidance and patience and for letting me be a part of the QDev family and entrusting me with such an interesting project. Thanks to Willy Chang, Andrew Higginbotham and Konrad Wolms for helping out at different stages of this process. A very special thanks goes out to Morten Arpdog Kjærgaard for his inspiring attitude, unwavering spirit and invaluable teachings and friendship that have pulled me though those easy and difficult times.

Contents

Abstract

This thesis is focused on fabrication and characterization of an InSb quantum well device. A Hall Bar device is manufactured and a Hall effect measurement is carried out. Values such as the electron density and the mobility are then extracted. The weak antilocalization peak is observed and the usual fitting model is shown not to apply to the data obtained. A rough estimation of spin-oribt energy is made from direct readout of the peak. Finally, a magnetic field applied in the plane of the quantum well was shown to destroy the weak antilocalization effect.

Chapter 1

Introduction and Motivation

This chapter aims at giving a very basic introduction to one of the big research areas of the Center for Quantum Devices: topological quantum computing and Majorana fermions. The last part of the chapter provides a short overview of the work presented in this thesis.

Quantum computers have been the subject of extensive research in both theoretical and experimental physics for several decades. The main idea behind these computers is exploiting quantum phenomena for information storage and manipulation, instead of conventional transistor bit-based computing. An example is forming superposition of the spins of an electron and utilizing them as qubits to perform faster computations. One of the major problems obstructing the realization of such quantum devices is decoherence. Decoherence involves loss of information about the state of the system because of its entanglement with the environment.

A topological quantum computer has been proposed as a solution to overcome decoherence[1]. Quantum information in this type of computer can be stored in a group of quasi-particles called Majorana fermions (MF). A MF can be thought of as "half" of an ordinary fermion, which means that a superposition of two MFs is required to construct a fermion. It is its own antiparticle and a pair of MFs has zero energy[2].

MFs are theorized to arise in certain solid state system setups. One of the proposals for such a system is a one-dimensional (1D) semiconductor wire coupled to a superconductor[3, 4, 5]. Some of the requirements for engineering such device are: 1D semiconducting wire with strong spin-orbit coupling (SOC), an external magnetic field aligned along the nanowire and an s-wave superconductor connected to the wire[6].

The one-dimensional confinement makes it easy to isolate a single mode needed to ensure the formation of only one MF at each end of the wire. The spin-orbit interaction present in the material breaks the spatial inversion symmetry of the carriers and causes splitting of the spin bands, thus lifting some of the spin degeneracy (Figure 1.1a). The external Zeeman field opens up a gap at the crossing of the split energy bands, providing a region free of spin degeneracy (Figure 1.1b). Larger Zeeman field forces the spins to align to the applied field (Figure 1.1c), making it difficult to induce superconductivity. The s-wave superconductor opens a gap around zero bias by inducing superconductivity in the wire via the proximity effect[7] (Figure 1.1d). A pair of localized MFs is then predicted to form, one MF at each end of the wire.This spatial separation protects the states from decoherence.

Indium Antimonide (InSb) is a promising semiconductor material for the realization of MF. In fact, some of the first potential signatures of MFs have been detected by Mourik and collaborators in InSb nanowires[6], although other explanations of the zero-energy states have been proposed [8]. Bulk InSb possesses SOC and a Landé g-factor of ≈ 50. This is around 3.5 times larger than in InAs (another material with strong SOC), and 100 times larger than in GaAs[9]. A large g-factor is important with regards to the applied Zeeman field, which has the energy of $E_z = g\mu_B B/2$, where g is the Landé g-factor, μ_B is the Bohr magneton and B is the external magnetic field. This means that materials with higher g-factors require lower magnetic fields to achieve the same Zeeman splitting as materials with lower g-factors. Superconductivity is suppressed by a magnetic field of some material dependent critical magnitude, so it is of significance to keep the Zeeman magnetic field as low as possible.

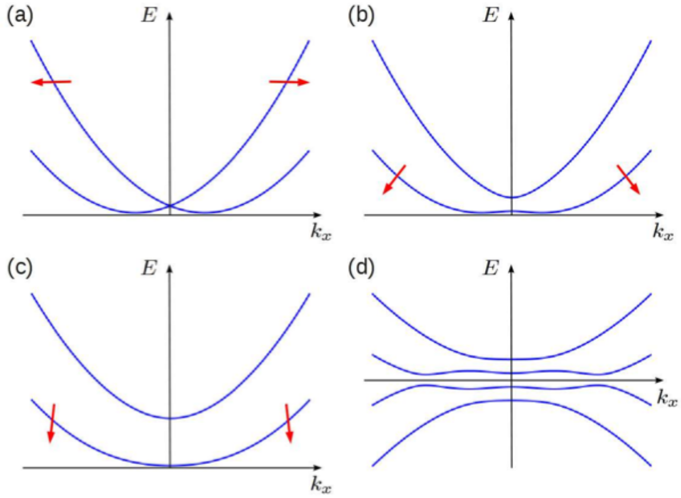

Figure 1.1: *Bandstructure of a 1D nanowire. a) Shifting of the two spin bands along momentum, k, due to spin-orbit coupling in the nanowire. b) The applied magnetic field creates an anti-crossing, producing a gap and thereby a spin degeneracy free region. c) A larger magnetic field opens a bigger gap, but at the same time forces the spins to align. d) Superconductivity induced by proximity effect. Figure taken from [7].*

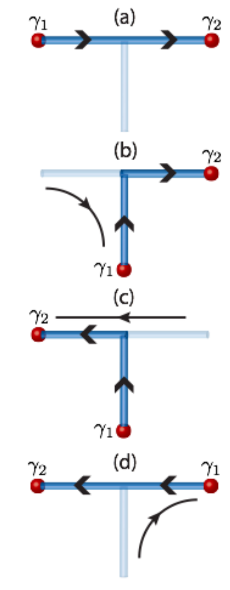

Figure 1.2: *T-junction composed of 1D nanowires proposed for Majorana braiding. a)-d) Showing the exchange of MFs (red dots) around eachother. Figure taken from [10].*

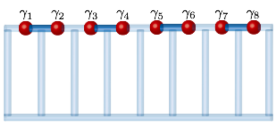

Figure 1.3: *A system of joined 1D nanowire T-junctions for exchange of several MFs. Figure taken from [10] .*

To perform computational tasks a manipulation of the qubit states must take place. Interchanging normal fermonic or bosonic particles does not lead to a change in their quantum state, because they are indistinguishable. MFs, on the other hand, obey non-Abelian statistics, which means that simply exchanging one MF around the other is going to drive the system to a new quantum state. This type of operation is called braiding.

A lot of the research has focused on realizing Majoranas in 1D nanowires[6]. But braiding in 1D is troublesome, since MFs have to be exchanged around each other. One possibility is creating a network of nanowires forming a T-junction (Figure 1.2) or several connected T-junctions, the so-called "ladder" configuration (Figure 1.3)[10].

The exchange is then performed by pushing one MF (indicated by red dot) at a time around the loop in four steps (indicated by arrows) with the help of gates. This method presents great device fabrication challenges. The task of manipulating nanowires is in general difficult because of their size. If this method is to be scalable, a numerous amount of nanowires is required, and the notion of manipulating each and every one in the very ordered fashion that the ladder confirmation demands seems strenuous and unsustainable.

The InSb group at this center focuses on InSb/AlInSb quantum well (QW) heterostructures instead. The goal is top-gating these heterostructures to pattern quasi-1D wires in the QW. This simplifies the design and fabrication process a great deal, since laying down a complicated network of the quasi-wires is easier and is achievable in equal amount of steps as laying down one.

The aim of this thesis is fabrication and characterization of symetrically doped InSb QW structures. The characterization is done by Hall and weak antilocalization (WAL) measurements. A WAL measurement is a tool used to estimate the spin-orbit energy. Finally, the impact of in-plane magnetic field on the WAL peak is studied. Chapter 2 contains a description of some of the material properties of InSb. Furthermore, the theory necessary for understanding SOC is presented, along with its relation to Landé g-factor and some of the quantum transport effects SOC gives rise to, namely WAL. Chapter 3 is a description of the fabrication of the Hall bar structures and experimental setup. The results of the Hall measurements is presented in Chapter 4. The strength of the spin-orbit and other relevant parameters is extracted from the WAL peak and the effect of the in-plane magnetic field on the peak is presented. Chapter 5 summarizes the thesis and provides ideas for future work.

Chapter 2

Theory

2.1 Indium Antimonide

Indium Antimonide (InSb) is a III-V semiconductor material. The crystal structure of InSb is zincblende, which consists of two face-centered cubic lattices, displaced along a diagonal from each other (Fig.2.1). The two sub lattices are made up from indium (group III) and antimony (group V), respectively. The lack of center of inversion in the zinc blende structure is a good choice for studying and exploitation of spin-orbit effect. InSb is a narrow band gap material, with low effective mass, strong spin-orbit coupling and a high g-factor, which makes it a suitable candidate for spintronic-based devices. A comparison between InSb values and some other popular III-V semiconductors is outlined in Table 2.1.

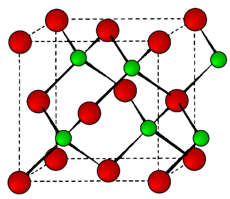

Figure 2.1: *InSb unit cell, displaying the zincblende structure. Green shapes correspond to indium atoms and red shapes to antimony atoms. Figure taken from [11].*

The InSb studied in this thesis is provided by the Naval Research Lab. It is grown by molecular beam epitaxy (MBE) on semi-insulating (100) GaAs. The wafer structure of InSb material is depicted in Figure 2.2. The InSb quantum well is 50 nm wide and sandwiched between 20 nm thick layers of $Al_{0.8}In_{0.2}Sb$. The QW is symmetrically doped with silicium atoms and buried 70 nm beneath the surface. An additional doping layer is added 20 nm beneath the surface to protect the QW from being affected by the surface states [12].

Property	InSb	InAs	GaAs
Electron g-factor	-51	-15	-0.44
Effective mass (m^*/m_0)	0.014	0.023	0.065
Energy gap (eV)	0.175	0.356	1.43
Dresselhaus coefficient (eV $\mathring{A}^3$)	760	27.2	27.6

Table 2.1: *Room temperature properties of common semiconductor materials: InSb, InAs, GaAs.*

2.1.1 Formation of Quantum Wells

Being able to confine charge carriers in one, two or three dimensions lies at the heart of fabricating and utilizing semiconductor-based devices. The confinement leads to formation of discrete energy levels in the direction of confinement, thus limiting carrier transport in the confined dimension, but allowing free transport in the other dimensions. In our case, the QW is formed by sandwiching a thin layer (50 nm) of InSb between the larger band gap material, AlInSb, see Figure 2.4.

The QW is doped with Si-atoms on both sides by the remote δ-doping technique. This means that a thin layer of Si-atoms is added to the plane during MBE growth a small distance away from the QW. The small bandgap of InSb makes it energetically favourable for the donors to 'spill

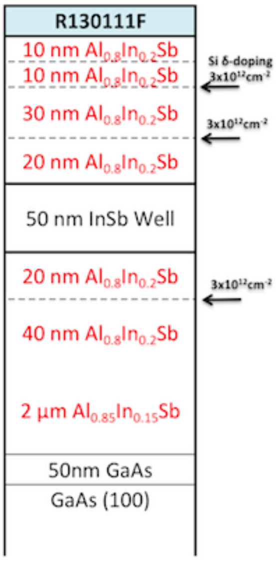

Figure 2.2: *Wafer structure of R130111F. R130111F is grown on (100) GaAs and consists of several layers of $Al_{1-x}In_xSb$ and a 50 nm wide InSb QW. The arrows indicate Si doping layers.*

over' from the larger gap AlInSb, thereby getting trapped at the interface in the InSb QW by the positively charged dopants.

This arrangement confines the carriers in the growth direction, allowing them to move only in the plane of the QW. AlInSb is used because of the relatively small lattice mismatch between AlInSb and InSb. This is important, because a large mismatch will create a big strain in the QW and result in increased scattering of the carriers and thus lower electron mobility.

The system is not truly a 2D system due to the small spatial extension of the QW in the growth direction. But it is a quasi-2D system as long as the width of the QW is comparable to the Fermi wavelength of the electrons, $\lambda_F \approx W_{QW}$, such that the quantization is apparent. Increasing the QW width much above this limit will smear out the discreetness, allowing for easily accessible energy states and thus ordinary 3D transport as in bulk material. The Fermi wavelength for the sample measured in this thesis is calculated in section 4.1 to be $\lambda_F \approx 23$ nm, which is the same order of magnitude as 50 nm and therefore the system is still considered 2D.

2.2 Spin-Orbit Coupling

Spin-orbit coupling is a relativistic effect arising from breaking of spatial inversion symmetry. It emerges from the coupling of the spin of the carrier to its orbital motion. The coupling can be derived as a relativistic correction from the Dirac equation, so the spin-orbit Hamiltonian is:

$$H_{so} = \frac{e\hbar^2}{4m_0^2c^2}\sigma(k_x \nabla V) \tag{2.1}$$

where m_0 is the free electron mass, c is speed of light, σ is vector of Pauli spin matrices, k is electron momentum and ∇V is the electrostatic potential of the nucleus. The electric field produced is the graient of the potential: $E = -\nabla V$.

A particle moving through an electric field will, from its own rest frame, feel the electric field as an effective magnetic field, due to the Lorentz transformation of E. This effective magnetic field will partially lift the spin degeneracy of the carrier.

Spin degeneracy in a semiconductor stems from a combination of spatial inversion and time reversal symmetry. Spatial inversion symmetry gives: E(k,↑)=E(-k,↑) and time reversal gives: E(k,↑)=E(-k,↓). Both operations transform k into -k and time reversal also inverts the orientation of the spin. That is, preserving time reversal symmetry means that when you reverse the velocities

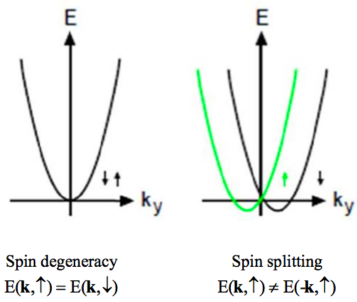

Figure 2.3: *Energy diagram of a spin degenerate state and the spin split state, where the spatial inversion symmetry has been boken. Figure taken from [12].*

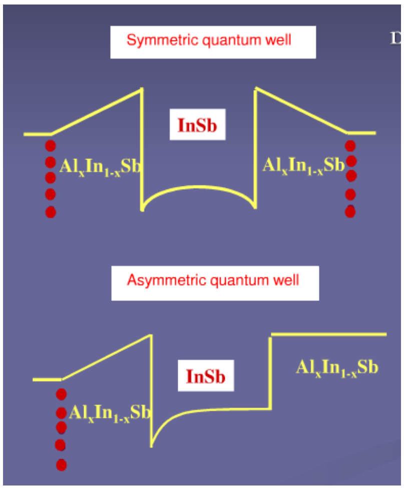

Figure 2.4: *Symmetrically and asymmetrically doped InSb QWs. The asymmetry creates bending of the energy band and gives rise to a potential gradient and an electric field in the growth direction of the QW. Figure is courtesy of Prof. Michael B. Santos from University of Oklahoma.*

of the system, it will go back to its initial state. The spatially spin-split states are degenerate at zero momentum, see Figure2.3.

SOC in semiconductors originates from two different effects: bulk inversion asymmetry (BIA), which is associated with the crystal structure of the bulk material and structural inversion asymmetry (SIA), which is related to the asymmetry in the doping profile of the heterostructure. The two effects are also known as Dresselhaus and Rashba, respectively.

Rashba term emerges due to an asymmetry in confinement potential of the QW, see Figure 2.4. This asymmetric doping creates a slope in the potential of the band profile, which corresponds to effectively having an electric field. In this case the field is pointing in the z-axis or the growth direction of the heterostructure. The Hamiltonian describing Rashba is $H_R = \alpha(-k_y\sigma_x + k_x\sigma_y)$, where α is a material-dependent constant and the sigmas, σ, are Pauli spin matrices.

Dresselhaus spin-orbit interaction comes from the inversion asymmetry of the crystal itself. As previously mentioned, InSb is a zincblende crystal structure. The lack of the center inversion symmetry of the structure creates an an effective internal electric field inside the crystal. There are two types of Dresselhaus contributions in 2-dimensional semiconductor systems. One is the cubic Dresselhaus, which dominates the bulk zincblende type semiconductor. The cubic term is due to the electron wave vector propagation in the three dimensions, k_x, k_y, k_z. The Hamiltonian is $H_D^{(3)} = \gamma(\sigma_x k_x k_y^2 - \sigma_y k_y k_x^2)$. The other term is linear and stems from confinement in k_z. When the Dresselhaus is applied in the (001) direction of the structure, the Hamiltonian for this type of Dresselhaus is $H(001)_D = \beta(-k_x\sigma_x + k_y\sigma_y)$, where β is intrinsic material dependent constant. For wide, heavily doped QWs, such as our sample, both Dresselhaus terms contribute and should be included in the analysis of spin-orbit interation [12].

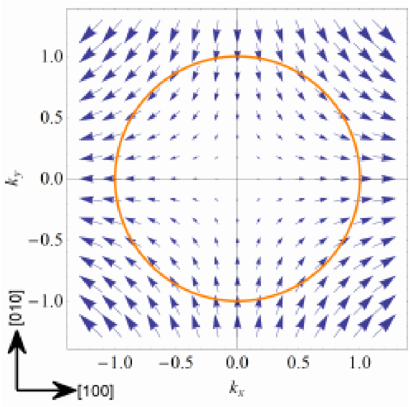

(a) Linear Dresselhaus field

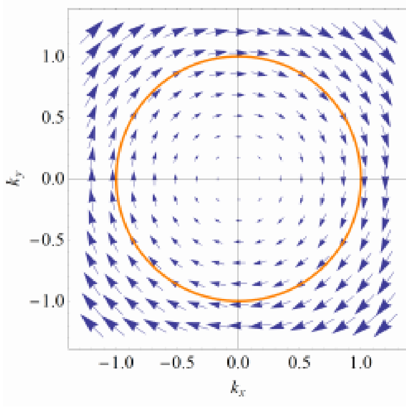

(b) Linear Rashba field

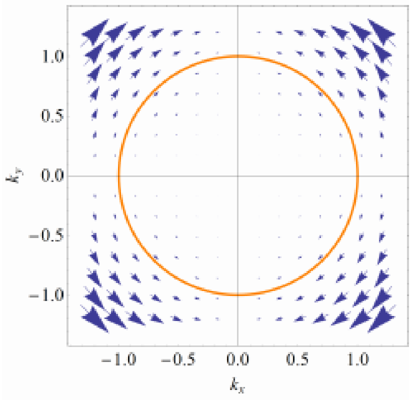

(c) Cubic Dresselhaus field

Figure 2.5: *Direction of the magnetic field (indicated by blue arrows) in 2D k-space produced due to the three different types of spin-orbit interaction: a) Linear Dresselhaus b) Linear Rashba c) Cubic Dresselhaus. Yellow circle outlines the Fermi sphere. Figure taken from [13].*

Figure 2.5 shows the effective magnetc field (blue arrows) in 2D k-space originating from linear Rashba and linear and cubic Dresselhaus terms.

Apart from the strong spin-orbit interaction, InSb is known for its large effective Landé g-factor, $g*$, which is around 50 in the bulk. SOC and effective g-factor are related phenomena. The g-factor is a constant describing how well the electron responds to the applied magnetic field. The g-factor of a free electron is approximately 2. As mentioned above, SOC couples the electron's orbit to the spin. If a magnetic field is applied, the orbital motion of the electron will change and it will exhibit Zeeman splitting, making the g-factor look larger.

2.3 Weak Localization and Weak Antilocalization

Weak localization is a phenomenon arising from phase coherent electron interference in disordered, low-dimensional systems with small or absent SOC.

Quantum mechanically, an electron traveling through semiconductor material in an electric field will exhibit wave-like behavior. In general, resistivity stems from the electrons encountering a number of scatterers while on their path through a crystal lattice. These encounters give rise to backscattering of the electron, leading to resistance. There is a certain probability that the partial wave of this electron can scatter in such a way that it takes the time-reversed path, such as it comes back to its origin, thus enclosing a loop (Figure 2.6). Because the distances traveled by the time-reversed paths are equal, the magnitude of the phase that the carrier has gained will be equal as well, leading to constructive interference between the trajectories and therefore enhanced backscattering.

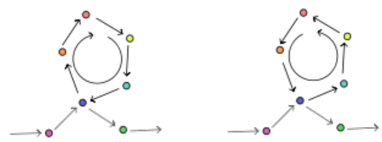

Figure 2.6: *Time-reversed trajectories of the partial waves of the electron, traveling clockwise and counter-clockwise. Figure courtesy of Wikimedia.*

The probability of return to the origin can be described by the amplitudes of the trajectories, A^+ for clockwise and A^- for counter-clockwise, which are equal due to time reversal:

$$|A^+ + A^-|^2 = |A^+|^2 + |A^-|^2 + A^+A^{-*} + A^{+*}A^- \tag{2.2}$$

The first two terms on the right side of the equation describe the classical probability, $P_{classical} = 2|A|^2$, and the last two terms, containing complex amplitudes, describe the quantum mechanical correction. Adding up the amplitudes gives a total probability:

$$P_{total} = 4|A|^2 \tag{2.3}$$

This shows a doubling in the classical return probability and therefore an increased tendency of the electron to 'localize' in low-dimensional systems, thus the term 'weak localization' [14].

Introducing an external, perpendicular magnetic field will suppress the weak localization effect, because the trajectories will collect an additional phase, Aharamov-Bohm phase. The probability is now modified to be:

$$|A^+(B) + A^-(B)|^2 = 2|A|^2 + 2|A|^2 cos(4\pi \frac{BS}{\Phi_0}) \tag{2.4}$$

where B is the magnitude of the magnetic field, S is the area enclosed by the trajectories and $\Phi_0 = h/e$ is the flux quantum. When B=0, cos=1 and the weak localization has its maximum. For small fields, a small phase difference will be collected, so the return probability will not change significantly and therefore the resistance is not varied much. For large fields, the phase factor will be large and the probability of returning to the origin will get small and resistance drop. This results in the characteristic peak in resistance shown in Figure 2.7 left.

Weak antilocalization occurs in systems with large spin-orbit coupling. The partial waves of the electron sill make up closed loops, but now the spin is being rotated along these trajectories due to SOC. The rotation of the spin along the two time-reversed paths will be in opposite directions, which leads to destructive interference at the origin and thus diminishing of the probability of backscattering compared to the classical case. There are a few characteristic scales that are important to think about when talking about antilocalization. Those are spin scattering time, τ_{SO} and spin-orbit length, l_{SO}. The former is a measure for the time before the spin flips and the latter

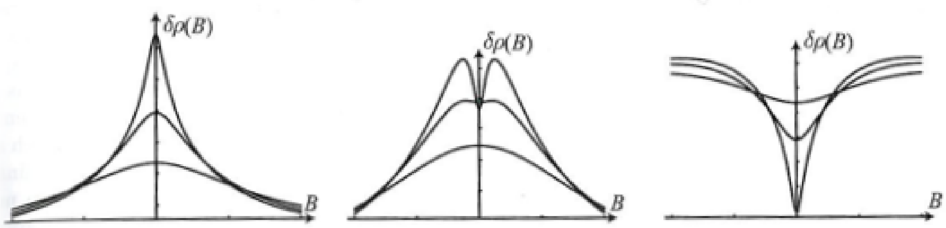

Figure 2.7: *Different types of localization effects for three different temperatures. Left: Weak Localization occurs in systems with absent or weak SOI and is seen as increase in resistivity around zero magnetic field. Middle: Intermediate SOC strength regime, where weak localization turns into weak antilocalization. Right: Strong SOC and pure antilocalization effect. Figure taken from [14]*

is the corresponding length. The two are related through the diffusion constant: $l_{SO} = D\tau_{SO}$. Another scale is momentum scattering time, τ_e, and the corresponding length, l_e. The scale most important to observe WL and WAL is phase coherence time, τ_ϕ, and length, τ_ϕ.

Strong spin-orbit interaction causes fast spin scattering times, which are shorter than the phase coherence time, $\tau_{SO} << \tau_\phi$, that leads to spin direction randomization and therefore weak antilocalization.

The above explanation of the effect of the magnetic field on the weak localization is similar for weak antilocalization. The phase differences collected by the trajectories will destroy the antilocalization effect and reveal the dip in the resistance (Figure2.7 right).

The shape of the peak or dip is controlled by the characteristic scales described above. Weak localization occurs when spin-orbit length is longer than the phase coherence length and both are longer than elastic scattering length or mean free path, $l_{SO} > l_\phi > l_e$. That is, the spin randomization is rare compared to the amount of scattering encountered, while phase coherence is still maintained between the scattering events. For weak antilocalization, spin orbit length has to be comparable to mean free path length, and smaller than the length when the coherence is lost: $l_{SO} = l_e < l_\phi$. In other words, the spin will be rotated between the scattering events, while phase coherence is maintained. In the intermediate incident, the spin scattering length will be larger than elastic scattering length, which means the spin will rotate less often between the scatterers. This yields the special case where the peak turns from weak localization into weak antilocalization (Figure 2.7 middle). If phase coherence is destroyed by, for example, increasing temperature, the peak will smooth out and the localization effects disappear (Figure 2.7). Spin-orbit field, B_{SO}, is the field where the turnover from WL to WAL occurs. It is related to the spin-orbit length by $B_{SO} = \phi_0/l_{SO}^2$. That is, the shorter the spin-orbit length and thus stronger SOC, the larger the spin-orbit field.

This shows that a magnetotransport measurement can be performed to estimate the strength of the spin-orbit coupling. The next chapter will describe the set-up for such a measurement.

2.4 In-Plane Magnetic Field

Applying a magnetic field parallel to a QW will quench the weak antilocalization effect. There are two reasons for this: one is the Zeeman effect and the other is QW microroughness [15]. Both contribute with additional dephasing of the carriers, losing the phase coherence required to observe WAL. For narrow QWs the effect of Zeeman interaction on the orbital motion is negligible and it mainly couples to the spin of the carriers. The other contribution is from roughness of the QW that disrupts its 2D nature. An applied in-plane magnetic field will then give rise to minor, random perpendicular components at these roughness points. This component will naturally have an effect on the orbital motion of the electron, just like described for the perpendicular field above. More in-depth discussion on in-plane field effect on WAL in QWs can be found in [15].

Chapter 3

Fabrication, Setup and Experiment

This section contains information about device fabrication, setup and measurements. Each fabrication step is described shortly, but detailed recipes are provided for each fabrication step in the appendix section.

A Hall effect measurement is used as a tool to characterize semiconductor material properties, such as mobility and density of a quantum well. Hall bar (HB) shaped devices provide an easy way to extract these parameters. The geometry of such a HB is a long and thin channel with enough contacts to perform a four-point measurement (Figure 3.2). This section focuses on fabrication of and measurement of such a device. The final device is shown in Figure 3.1. The theory behind the Hall Effect, the reason for this type of geometry and other possible device shapes is explained in-depth in chapter 10 in reference [14].

The sample fabrication process includes several steps. Those are optical and electron beam lithography, Kaufman source ion milling, metal deposition and annealing.

The fabrication process begins with cleaving the wafer in the desired dimensions with the scriber, in our case 5.3×4.9 mm. The scriber can apply different force and we found out that using the pre-marked setting for silicon and scribing twice across the wafer makes perfect cuts in InSb.

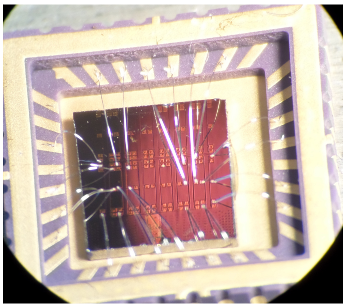

Figure 3.1: *Optical image of device R130111F.4, which contains 14 HBs, glued and wirebonded to a chip carrier, ready for cooldown*

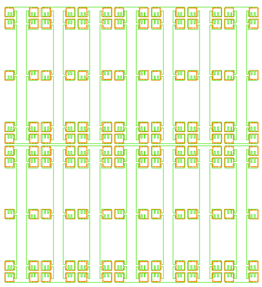

Figure 3.2: *Design CAD Hall bar pattern used for electron-beam lithography.*

The crystal orientation of this sample is unfortunately lost.

Lithography requires application of photoresist, a light sensitive material, onto the sample. Photoresist is different type of plastic materials consisting of long polymer chains, which are sensitive to certain wavelengths of light. Once exposed to this certain type of light the chemical bonds of the polymer will be broken and a pattern can be developed. The lithography process is sensitive to contamination, so the photoresist application and optical lithography step are carried out in the cleanroom.

Optical lithography is used for transferring patterns with features larger than a micron. The size of Hall bars fabricated for this thesis is 2000×500 μm, which makes optical lithography a suitable technique, resolutionwise. The exposure is performed through a patterned metal mask with SUS MJB-3 UV mask aligner which has a 200W mercury lamp that transmits light with wavelengths around 365 nm. The exposure time depends on the resist type, feature size and intensity of the lamp. A chemical called 'developer' is used to remove the broken polymer chains and develop the pattern.

The next fabrication step is to isolate the QW in the HB geometry outlined above. This is done by dry etching or "milling" away material with the help of a Kaufmann Ion Source. A Kaufmann ion source is built in AJA system 1 and is normally used to polish sample surfaces to remove oxide layers. The sample is placed in high vacuum chamber and a plasma is created by ionizing argon gas. The charged ions are then accelerated through a tungsten filament, which provides space-charge neutralization. The accelerated argon ions will then hit the surface, thereby mechanically removing material. The Kaufmann source will remove both the photoresist and the InSb material left unprotected after developing the resist. It is sufficient to mill just under the QW. The mill rates for both InSb and the photoresist are around 15nm/min.

To be able to manipulate the isolated QW in the HB structure, electrical contact has to be established. The first step is to pattern out the contacts, which requires another lithography round. Electron beam lithography (EBL) makes use of high voltage, in our case 100kV, to accelerate electrons and directly write features in the resist. The desired pattern is created in design software, which makes the system more versatile compared to pre-made metal mask solution of UV-lithography. EBL is normally used for patterning small, sub-micron sized features, but is here used to define device contacts, which are 150 x 150 μm in size. This would be easy to do with UV light, but the mask with contacts corresponding the the hall bar mask could not be located. The system used for EBL is Elionix ELS-7000. A double layer of different type of resist is often used for EBL, if the next fabrication step is metal deposition. Due to differences in chemical composition of the two types of resist (the first layer being more reactive than the second), an undercut will be created under the upper resist layer after development, aiding future metal liftoff. See full recipe Appendix B.

The second step is depositing metal in the exposed contact areas. The deposition is performed by evaporation in either AJA system 1 or 2. The materials used for ohmic contacts are thin layers of palladium, platinum and gold. The recipe is provided by Brad Boos from the Naval Research Lab (see details in Appendix C), which they use for Sb-based High-Electron-Mobility-Transistors to yield low contact resistance. We have tried using Ti/Au as contact materials, without success, although we did not try annealing.

The sample is once again placed in vacuum and an electron beam is used to heat up and eventually melt the material of choice. After reaching a certain temperature, the material will evaporate and condense, forming a thin, uniform film layer covering the sample. The sample is then placed in a solvent that dissolves and removes the photoresist along with the thin film deposited on the top of the resist, leaving only the material in contact with bare InSb surface behind.

The final fabrication step is annealing and we use the Rapid Thermal Annealer AW610 for this. The purpose of annealing is heating of the deposited material, thereby forming tendrils that diffuse into the sample, establishing ohmic contact to the QW. Ohmic contact means a linear relationship of the voltage applied, versus the current achieved between the semiconductor-metal interface, which is necessary for material characterization. A number of semiconductor-based devices require non-ohmic contact, such as a Schottky diode, which exhibits rectifying behavior depending on the direction of current applied.

The Rapid Thermal Annealer utilizes high energy lamps for heating purposes and it has the ability to raise its chamber temperature to several hundred degrees Celcius in a matter of seconds and

rapidly cool it again. A different number of process gases can be used to alter the annealing process. The annealing recipe is provided in Appendix D.
Annealing for example GaAs requires short, few second bursts of very high temperature (up to 1000°C). InSb wafer structures are, on the other hand, grown at temperatures around 350°C, which means it is important not to go above this to retain the grown structure. This limits the choice of contacting material, since the melting point of these has to be below the growth temperature. Sheena Murphy, associate prof. at University of Oklahoma, suggested using a thin layer of indium and a few minutes of low temperature annealing. This should be worth trying out in the future, since it shortens the deposition and especially the annealing time significantly.

3.1 Experimental Setup

3.1.1 Hall Measurement

In this experiment a four-point measurement is performed. This means sourcing a current between two contacts and measuring a voltage drop across two other contacts. Due to the large impedance in the voltage probe, its contribution can be neglected and the voltage readout will be only the resistance of the area between the two voltage probes.

One type of four-point measurement is a Hall measurement. It involves sourcing a current from one end of the HB to the other and measuring a voltage drop along the HB (longitudinal voltage) and across the HB (Hall voltage), while sweeping the perpendicular magnetic field. An overview of the setup is depicted in Figure 3.3a and Figure 3.3b.

The R130111F.4 consists of 14 HBs: two rows of sevel HBs in each row. The upper row are all dead devices. The lower row is numbered 1-7 from left to right. Device 1, 2, 6 and 7 are wire bonded (Figure 3.1 and 3.2). HB 1 and 6 turned out to have some bad ohmic contacts, which made it impossible to perform four-point measurements. The data presented in this thesis is taken from measurements on HB7.

A lock-in amplifier (SR830 from Stanford Research) is used as a voltage source, sourcing 0.1V. A large resistor of 10 $M\Omega$ is placed before the source contact. This resistance is chosen to be larger than sample and line resistances combined to ensure a constant, small current through the sample. According to Ohm's Law, $I = V/R$, this results in a current of 10nA through the sample. The current is kept low at 10 nA to prevent heating of the electrons. The voltage drop is measured as indicated in Figure 3.3a and 3.3b. Contacts not in use during the measurement are set to 'float' on the breakout box to ensure that all current is flowing to the designated gorund. The voltage probe BNC cables are arranged in a twisted pair fashion, i.e. twisted around each another, to minimize background noise. The perpedicular magnetic field is swept from 500 mT to -500 mT, at a ramp rate of 60mT/min in 1000 steps with a 1.1 second waiting time between steps, which ensures the magnet has ramped to the set value and has had time to settle. The lock-in frequency setting is 318Hz. This frequency has recently been checked with a spectrum analyser to confirm low backgroud noise.. Longitudinal and Hall voltages are measured separately.

The measuring and cooling of the sample takes place in a cryo-free dilution refrigerator (Triton 1) of the type Triton 200 from Oxford Instruments. The data is taken at fridge mixing chamber temperature of 33 mK

3.1.2 In-Plane Magnetic Field

Triton 1 provides a vector magnet with magnitudes X:1T, Y:1T, Z: 4T, which makes it suitable for sample measurements requiring different combinations of magnetic field directions. The sample is placed face down inside the sample puck using parallel mounting bracket, which results in the magnet axis orientation depicted in Figure 3.4. The rest of the setup is identical to Figure 3.3a. The goal is to repeat the four-point measurement from before, i.e. sourcing a current of 10 nA from the lock-in amplifier and measuring the longitudinal voltage drop across the HB, while applying a perpendicular magnetic field, $B_{\perp}$. Here we also sweep the in-plane magnetic field, $B_{||}$, at the same time.

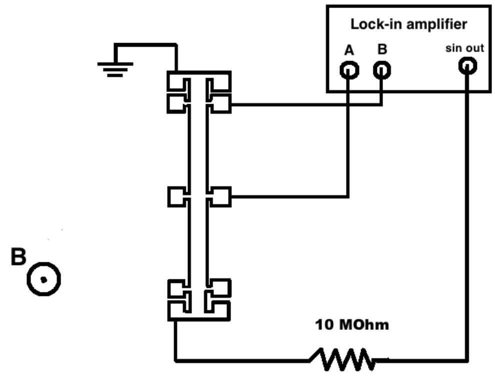

(a)

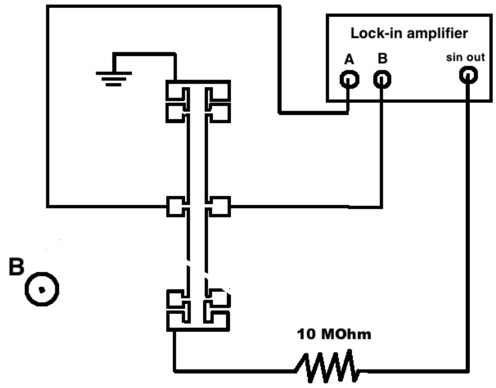

(b)

Figure 3.3: *Setup for Hall measurements. A lock-in amplifier is sourcing 0.1 V through a* $10m\Omega$ *resistor, yielding a current of 10 nA through the sample. A magnetic field is applied perpendicular to the HB. (a) shows the longitudinal measurement (voltage probes arranges along the HB) and (b) shows the Hall measurement (voltage probes arranged across the HB).*

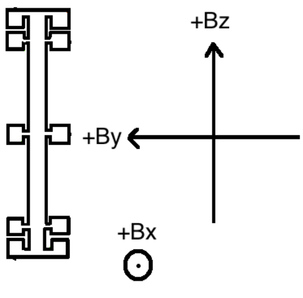

Figure 3.4: *Orientaition of the HB with respect to the vector magnet inside Triton 1. Positive perpendicular magnetic field,* $B_{\perp}$*, corresponds to* $+Bx$ *and* $+By$ *equals the positive applied in-plane magnetic field,* $B_{||}$*.*

Chapter 4

Data Presentation and Analysis

4.1 Hall Measurement

The data from the Hall measurement performed on HB7 on device R130111F.4 is shown in Figure 4.1. It shows two curves: a Hall voltage measurement (red V_{xy} curve) and a longitudinal voltage measurement (blue V_{xx} curve). The two measurements are done separately.

The Hall voltage exhibits a linear relationship between the applied magnetic field and the built up voltage across the HB. The longitudinal measurement shows a sharp, pronounced drop in voltage around zero magnetic field of about 0.5 μV in magnitude. This dip is a signature of weak antilocalization effect and will be addressed in the next subsection. The 'wings' extending from the dip also show a slight drop and rise in voltage, though it is spread out over several millitesla and can be considered almost linear. The asymmetry of the wings around zero magnetic field is found to be dependent on the direction of the magnetic field sweep. While sweeping from positive field to negative field, the drop of the left wing is deeper and the other way around. This can potentially be avoided to some extent by decreasing the magnet ramp rate and increasing the waiting time. To check whether the asymmetry is temperature-dependent , the mixing chamber temperature could be increased and the measurement repeated.

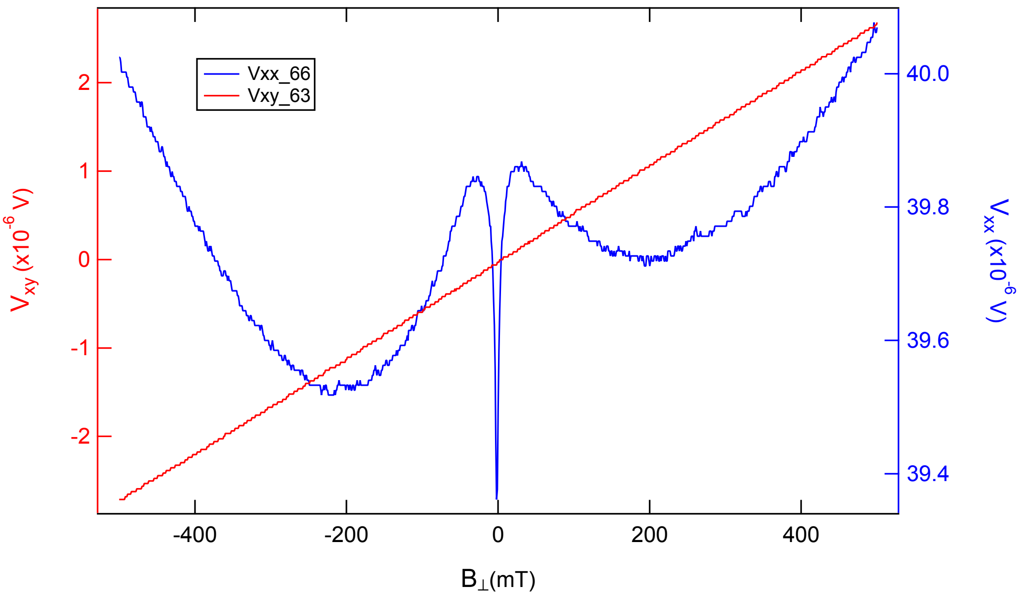

Figure 4.1: Result of the Hall measurement, voltage as a function of perpendicular magnetic field. Red curve, V_{xy} is the Hall voltage and blue curve, V_{xx}, is longitudinal voltage. The applied current is 10 nA.

The electron density of the sample can be extracted from the slope of the Hall voltage, according to equation:

$$n = \frac{IdB}{|e|dV_{xy}} \tag{4.1}$$

where I is the current through the sample, $|e|$ is the elementary charge and dB/dV_{xy} is the gradient of the Hall voltage vs. the magnetic field, B. Fitting a straight line to the slope and inserting the numbers yields an electron density for the sample of $n = 1.2 \cdot 10^{12}\ cm^{-2}$.
The mobility, μ, is calculated from the longitudinal voltage:

$$\mu = \frac{I/|e|}{n\ V_{xx}\ W/L} \tag{4.2}$$

where V_{xx} is the longitudinal voltage and W/L is the width and length ratio of the HB between the voltage probes, which in this case is 1/5. The readout of V_{xx} is done in the middle of the wing to obtain the average value. It can also be done at the bottom of the wing, but the voltage varies approximately $0.4\mu V$ over the length of the measurement, so the result is not affected significantly. Inserting numbers gives a sample mobility of $\mu = 6700\ cm^2/Vs$.

The methods and equations for extracting different parameters from Hall measurement are presented in Appendix E.

Table 4.1 shows some of the extracted Hall parameters compared to the measurements on similar InSb structures done by Dilhani Jayathilaka on sample t340 in reference [12]. It can be noted that the carrier density in R130111F is a factor of ten higher than in t340. The mobility is also decreased by a factor of ten in R130111F compared to t340. Some of the decreased mobility can also be explained by the different QW widths. Our 50 nm QW system is wider compared to the 20 nm QW of t340. This means less confinement in two dimensions and it will result in more electron scattering compared to a more pure 2D system, because of the strained QW.

Sample	QW (nm)	$n(cm^{-2})$	$\mu(cm^2/Vs)$	$\rho_{xx}(\Omega)$	$k_F\ (m^{-1})$	$l_e(\mu m)$	τ_e (s)	D (m^2/s)
R130111F.4	50	$1.2 \cdot 10^{12}$	6700	800	$2.7 \cdot 10^8$	0.12	$5.4 \cdot 10^{-14}$	0.134
t340	20	$4.0 \cdot 10^{11}$	48000	-	$1.6 \cdot 10^8$	0.47	-	-

Table 4.1: *Comparing values extracted from the Hall effect measurements. Comparasion is between measurements on the 50nm wide QW (R130111F.4) and the numbers from Dilhani Jayathilaka's PHD thesis and the 20nm QW HBs (t340). Compared values are QW width, electron density (n), mobility (μ), sheet resistivity (Ω), Fermi wavevector (k_F), mean free path (l_e), elastic scattering time (τ_e) and diffusion constant (D). See Appendix E for equations. Empty fields indicate insufficient information to extract the values.*

The orientation of the sample inside the sample holder only allowed for measurement with 1T magnet. No Shubnikov-de Haas (SdH) oscillations were observed up to the field of this magnitude. SdH oscillations arise from the quantization of energy levels, called Landau levels (LL), at certain strength of magnetic fields. LLs are signatures of the Quantum Hall Effect (more about this in [16]). The criterion for formation of LL is that the electron in the presence of a magnetic field completes a few orbits before scattering off impurities. This criterion can be summed up in $B >> \mu^{-1}$. That is, the higher the sample mobility, the lower the magnetic field where the oscillations become visible. The mobility of this sample is $\mu = 6700 cm^2/Vs$, that gives $B >> 1.5T$, which explains the missing oscillations in the measurements.

4.2 Weak Antilocalization

Figure 4.2 shows the conductance as a function of perpendicular magnetic field. The V_{xx} data from Figure 4.1 has been converted to conductivity curve in units of conductance quantum, e^2/h, according to convention. This is done by converting the voltage measurement to resistivity $\rho_{xx} = \frac{V_{xx}}{I}\frac{W}{L}$. Resistivity, ρ_{xx}, can be converted to conductivity, σ_{xx}, according to classical Drude model [16]:

$$\sigma_{xx} = \frac{\rho_{xx}}{\rho_{xx}^2 + \rho_{xy}^2} \tag{4.3}$$

where ρ_{xy} is resistivity obtained from the Hall voltage, $\rho_{xx} = \frac{V_{xy}}{I}$. If ρ_{xy} is small compared to ρ_{xy}, as in this case, its contribution can be ignored and equation 4.3 becomes:

$$\sigma_{xx} \approx \frac{\rho_{xx}}{\rho_{xx}^2} = \rho_{xx}^{-1} \tag{4.4}$$

which means it is sufficient to invert the resistivity data. Plotted on Figure 4.2 is $\Delta\sigma_{xx} = \sigma_{xx}(B) - \sigma_{xx}(0)$.

According to [14], mobilities below 10 m^2/Vs makes it easy to observe WAL peak in 2D electron systems. The mobility of this sample is 0.673 m^2/Vs, well under the criterion.

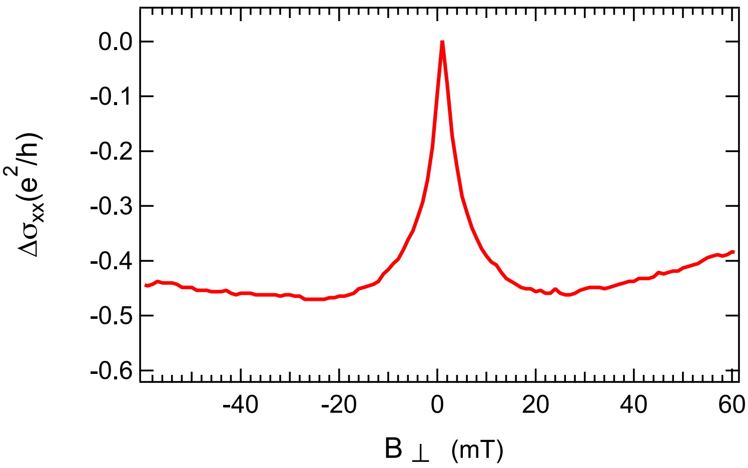

Figure 4.2: *Conductance as a function of perpendicular magnetic field, displaying the weak antilocalization peak centered around zero field. The turnover field or B_{min} occurs at 22.8 mT.*

The turnover field of the peak occurs at $B_{min} = 22.8mT$. This value is much larger than presented in the litterature for InSb, such as [12], who measure a turnover field of 1.2 mT for the HB structures.

4.2.1 Fitting

To extract information, such as spin-orbit energy and phase coherence length, from the WAL peak several fitting models can be employed. The theoretical model of choice depends on the type of spin-orbit interaction present in the sample and the transport nature of the system.

Hikami, Larkin and Nagaoka (1980) were the first to propose a theoretical model to describe WAL in bulk metal, where the cubic Dresselhaus term is the main contributor [17]. More advanced models have since then been presented, which take both Rashba and Dresselhaus terms into account, usually one linear term at a time: either Rashba or linear Dresselhaus. Among those is Iordanskii-Lyanda-Pikus (ILP)[18]. ILP model is developed to describe diffusive semiconductor material systems, where both Dresselhaus terms dominate. Since our QW is symmetrically doped, no Rashba term will arise and the ILP model seems to be sufficient for analysis of our WAL data. For more details on the theoretical model and the fitting parameters see [12]. The model is also only applicable to diffusive systems, that is, systems where the scattering length is shorter than magnetic length: $l_e \leq l_m$ and $l_m = \sqrt{\hbar eB}$, where B is the turnover field from WAL to WL. Inserting numbers gives a magnetic length of $l_m = 0.26\mu m$, which is larger than $l_e = 0.12\mu m$, indicating a diffusive regime.

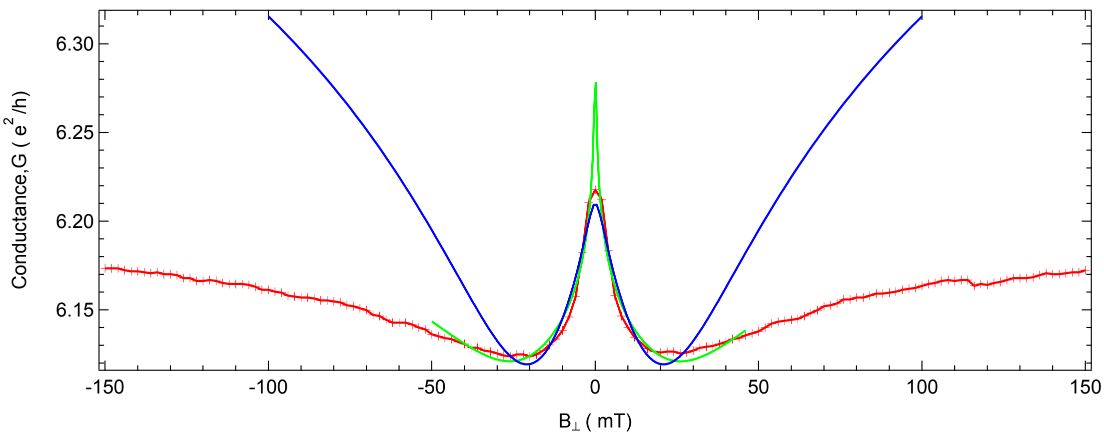

Figure 4.3: *Best fits attained with the ILP model. Conductance as a function of perpendicular magnetic field. Red curve is the WAL data, blue curve is the best fit around the WAL peak and green curve is best fit around B_{min}. This shows that no good combined fit could be achieved.*

Figure 4.3 shows the best fit attained by applying the ILP model to the WAL data (red curve). Two fits are attempted: blue curve shows the best fit around the WAL peak and the red curve is the best fit around B_{min}. The height of the peak is controlled by the phase coherence. It might then seem that information on phase coherence might be extracted, because the ILP model fits around the peak, but a different range of phase coherence values were tested out and many of them yielded a good fit around the peak, with changing of the incline of the wings. Therefore, no information about phase coherence can be obtained, except that it must be larger than both the spin-orbit length and scattering length, since the WAL feature is so pronounced. The region of WAL where the turnover occurs is fit as well, but yielding a poor fit around the peak. This deems the ILP model useless for this data.

Figure 4.4 shows the number of iterations, N, for the different magnetic field strength parameters required before the ILP equation converges. It shows a large difference in number of iterations and therefore care must be taken when applying the model to the data.

Studenikin et al. [19] show that ILP model cannot be applied to systems with strong SOC. Figure 10 in [19] shows a similar ILP theory fit to their data. Their WAL data resembles our data by the shallow steepness of the "wings" extending from the WAL to WL turnover point. The ILP is similar to the blue curve in Figure 4.3, that fits around the WAL peak, but not for the rest of the data at larger fields. The shape of our WAL data is in good agreement with the theoretical shape of WAL caused by strong SOC, shown in Figure 2.7 and explained in the theory section.

The authors then point out that it is suffiecient to determine the strength of the spin-orbit

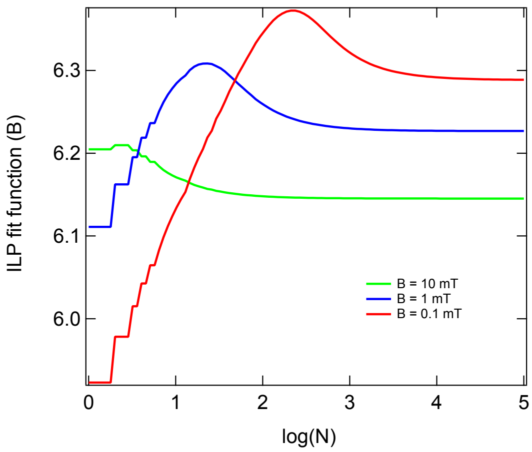

Figure 4.4: *ILP model as a function of log(N), where N is the number of iterations. The figure shows the number of iterations required for the ILP model to converge, for three different guesses on magnetic field fit parameter.*

the readout of the turnover from WAL to WL or B_{min}, that is $B_{so} \approx B_{min}$. This is claimed to be correct within $\leq 10\%$ error. The turnover in this sample happens at 22.8 mT. The spin-orbit energy can be extracted from the spin-orbit field by:

$$B_{so} = \frac{2\Delta^2 \tau_{tr}}{4eD\hbar} \tag{4.5}$$

where Δ is the spin-orbit energy, τ_{tr} is the transport scattering time and $D = l^2/2\tau$ is the diffusion constant. Inserting the values calculated and presented in Table 4.1 gives a spin-orbit energy of 9.1 meV. This value of spin-orbit energy is $\approx$ six times higher than for similar structures measured in [12]. This can be explained by the t340 has weaker SOC being in the intermediate SOC regime, which can be seen both from the shape of the WAL peak, where WAL peak abruptly turns over to WL, and also from the values obtained for mean free path and spin-orbit length ($l_{so} > l_e$). Spin-orbit length can be extracted from $B_{so} l_{so} = \frac{h}{2e} \leftrightarrow l_{so} = \sqrt{\frac{h}{2eB_{so}}}$, which gives $l_{so} = 0.26\mu m$. This is also slightly longer than the scattering length, which indicates a regime between intermediate and strong SOC.

Equation (4.5) is used in [19] to extact spin-orbit energy for a system with dominating Rashba term, which might make it unapplicable to our Dresselhaus-dominated QW.

This type of estimate makes it impossible to separate the contribution from linear and cubic Dresselhaus terms.

4.3 In-Plane Magnetic Field

A vector magnet allows for studying the effects of in-plane magnetic field on WAL. Figure 3.4 shows the orientations of the magnetic field with respect to the HB.
The data was taken at magnetic field sweep rate of 140 mT/min. The field was swept from $-150mT$ to $150mT$ in 150 steps with a 1.1 second waiting time. This was done for every $2°$ from $0°$ to $180°$, resultning in 90 steps.

Figure 4.5 shows a 2D plot of, what ca be interpreted as an effective rotation of the magnetic field of magnitude B_r in the xy-plane of the sample at angles θ. The conductance is measured for each θ at fixed magnetic field magnitude. The bright portions around $B_r = 0mT$ display increase in conductance. Thus, taking cuts through the plot for each angle will produce a WAL feature similar to previous measurement described above: with a conductance peak around $B = 0mT$ and a conductance minimum at some small magnetic field (darkest parts of the 2D plot) and again a small increase in conductance at each end of the 'wing' (the brighter parts from around $|B_r| = 50mT$). The widest WAL feature is seen at the angle of around $\theta = 90° - 93°$, that is, in

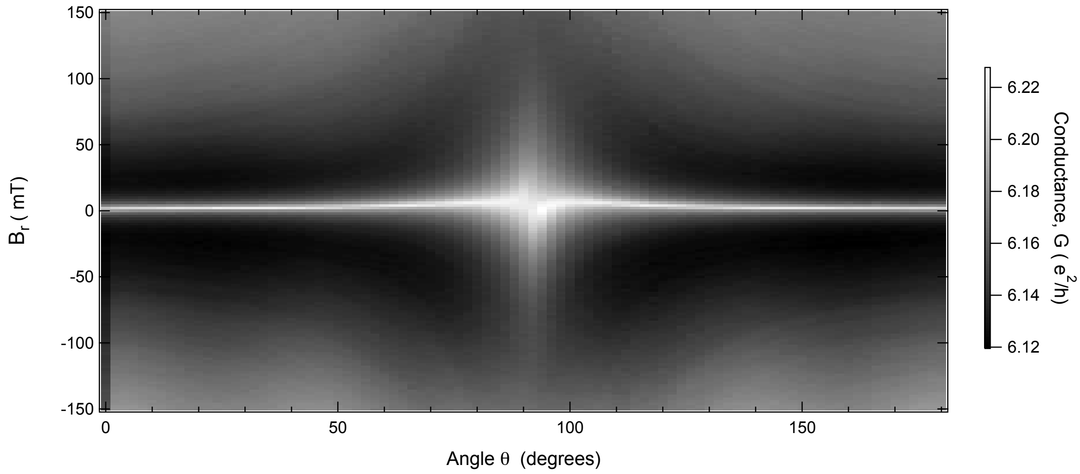

Figure 4.5: *A 2D plot of the magnetic field, B_r, as a function of angle θ with respect to xy-axis of the HB. The colourscale plot shows the conductance, G.*

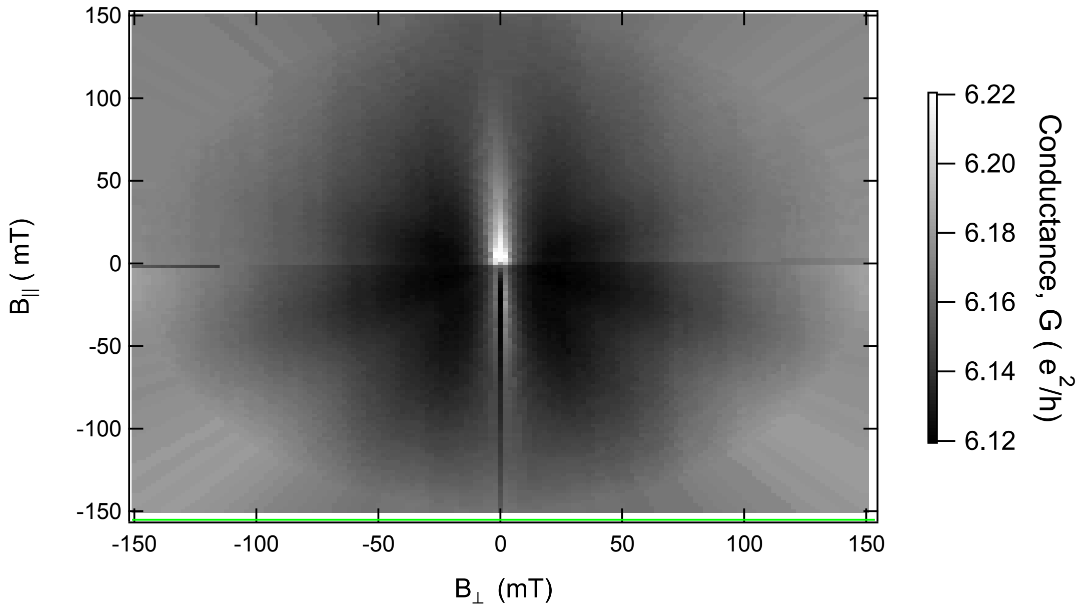

Figure 4.6: *This graph shows the data from Figure 4.5 replotted. It is a 2D plot of the perpendicular magnetic field against the parallel magnetic field, tracing an oval. Each perpendicular cut will therefore result in a graph of constant perpendicuar field sweep from $-150mT$ to $150mT$ for different parallel field magnitudes. The resolution of the data is determined by the oval circumference.*

pure parallel field with respect to the QW and perpendicular field, $B_\perp = 0$ The displacement of the WAL feature from $\theta = 90°$ indicates a small tilt of the sample.

We want to examine the effect of the parallel field on the WAL feature at fixed perpendicular magnetic field. To be able to see this, the data must be converted accordingly. For each angle from $\theta = 0°$ there is a slight decrease in $B_\perp$ and a corresponding increase in $B_{||}$. In that way, a circle can be traced with $B_\perp$ on the x-axis, $B_{||}$ on the y-axis and conductance in the third axis, as shown in Fig. 4.6. A cut can now be made through the $B_{||}$, parallel to $B_\perp$, giving a WAL peak for different magnitudes of parallel magnetic field at fixed perpendicular fields.

Figure 4.7 displays a number of these cuts stacked on top of each other for comparison purposes, separated by 0.05G. It shows a gradual reduction of the depth of the WAL peak with increase of the applied in-plane magnetic field. The dip in the WAL peak at $B_{||} = 0mT$ is some error in measurement, is not observed in previous or later stages and can therefore be ignored. The wiggly and distorted nature of the lines is attributed to bad 'resolution' of the measurement, where the data was acquired for each 2°. This resolution gets even worse for larger $B_{||}$ fields, because of further reduction in the number of data points, as seen on Figure 4.6. Nevertheless, it is clear that the WAL peak disappears at around $B_{||} = 140mT$.

As described in theory section, the in-plane Zeeman magnetic field couples to the spin of the carriers and contributes with a dephasing term, disrupting the coherent scattering required to observe the WL/WAL phenomena. As the carriers lose phase coherence, the WAL feature broadens out and decreases in height, until it can no longer be observed. As proposed by Minkov et al. [15], the Zeeman field is not enough to explain all of the dephasing present and the authors mention microroughness of the QW as another reason. Unfortunately, as we cannot fit a model to our data, it is impossible to tell, which effect contributes with what magnitude.

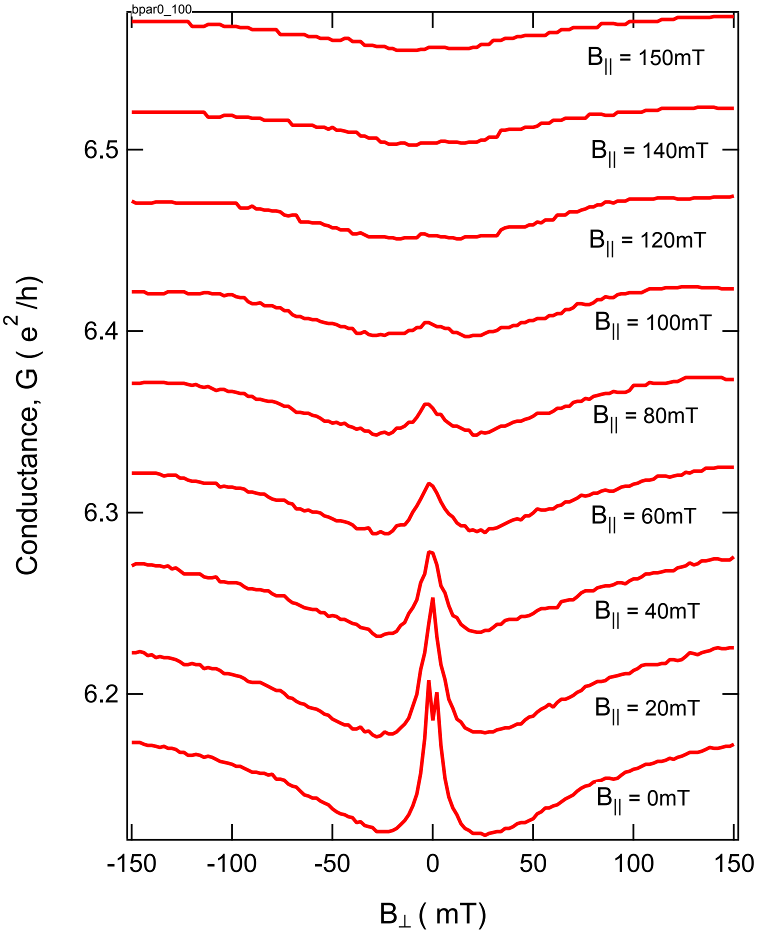

Figure 4.7: *Conductance, G, as a function of perpendicular magnetic field, $B_\perp$. The WAL measurement is shown for different values of in-plane magnetic field, $B_{||}$, from 0mT to 150 mT, separated vertically by 0.05G. This shows a gradual disappearance of the WAL feature with increasing strength of parallel field.*

Chapter 5

Conclusions and Outlook

The aim of this thesis was to fabricate Hall bar devices on AlInSb/InSb heterostructures and to characterize the structure by Hall effect and weak antilocalization measurements. The fabrication process included optical lithography, electron beam lithography, Kaufmann ion source milling, metal evaporation and annealing. Four-point measurements were performed on the fabricated Hall bars and parameters from Hall effect were exracted. Our sample showed low mobility, which is a criterion for observing the weak antilocalization signature - the peak in conductance around zero magnetic field. As it turned out, the ILP model could not be fitted to the WAL peak, but rough estimates of the spin-orbit energy could be performed. It was also shown that the parallel magnetic field destoyed weak antilocalization effect, due to both Zeeman effect and quantum well microroughness. It was not possible to establish how much each effect contributes.
Interesting things to investigate in the future could be spin-orbit interaction for different crystal directions and narrower quantum wells, which should give a larger spin-orbit energy. Also, in pursuit of the quantum information processing mentioned above, fabricating and characterizing patterned quasi-1D wires in similar InSb heterostructures is of great interest.

Bibliography

[1] Michael H Freedman, Alexei Kitaev, Michael J Larsen, and Zhenghan Wang. Topological Quantum Computation. arXiv.org, January 2001.

[2] P W Brouwer. Enter the Majorana Fermion. Science, 336(6084):989–990, May 2012.

[3] Jason Alicea. Majorana fermions in a tunable semiconductor device. arXiv.org, December 2009.

[4] Roman M Lutchyn, Jay D Sau, and S Das Sarma. Majorana Fermions and a Topological Phase Transition in Semiconductor-Superconductor Heterostructures. arXiv.org, February 2010.

[5] Yuval Oreg, Gil Refael, and Felix von Oppen. Helical liquids and Majorana bound states in quantum wires. arXiv.org, March 2010.

[6] V Mourik, K Zuo, S M Frolov, S R Plissard, E P A M Bakkers, and others. Signatures of Majorana fermions in hybrid superconductor-semiconductor nanowire devices. Semicond.Sci.Tech., cond-mat.mes-hall, 2012.

[7] Martin Leijnse and Karsten Flensberg. Introduction to topological superconductivity and Majorana fermions. Semicond.Sci.Tech., 27:124003, 2012.

[8] Eduardo J H Lee, Xiaocheng Jiang, Ramon Aguado, Giorgos Katsaros, Charles M Lieber, and Silvano De Franceschi. Zero-bias anomaly in a nanowire quantum dot coupled to superconductors. arXiv.org, July 2012.

[9] D. W. Palmer. Properties of the iii-v compound semic0nductors.

[10] Jason Alicea, Yuval Oreg, Gil Refael, Felix von Oppen, and Matthew P A Fisher. Non-Abelian statistics and topological quantum information processing in 1D wire networks. arXiv.org, June 2010.

[11] 08 2013.

[12] P.A. Renuka Dilhani Jayathilaka. Weak Anti-Localization Studies of Spin-Orbit Coupling in n- and p-type InSb Heterostructures. PhD thesis, University of Oklahoma, 2012.

[13] Leon Camenzind. Q u a n t u m t r a n s p o rt s i g n at u r e s o f e l e c t r i c d i p o l e s p i n r e s o n a n c e n e a r t h e p e r s i s t e n t s p i n h e l i x i n gaas quantum transport signatures of electric dipole spin resonance near the persistens spin helix in gaas quantum wells. Master's thesis, University of Basel, 2012.

[14] Thomas Ihn. Semiconductor Nanosctrucutres. Oxford, 2011.

[15] G M Minkov et al. Weak antilocalization in quantum wells in tilted magnetic fields. un, 2003.

[16] Supriyo Datta. Electronic Transport in Mesoscopic Systems. Cambridge University Press, 1997.

[17] Y. Nagoaka S. Hikami, A. Larkin. Spin-orbit interaction and magnetoresistance in the two dimensional random system. Prog. Theor. Phys., 63, 1980.

[18] G. E. Pikus S. V. Iordanskii, Yu. B. Lyanda-Geller. Weak localization in quantum wells with spin-orbit interaction. JETP Lett., 60, 1994.

[19] G. Yu S. A. Studenikin, P. T. Coleridge and P. J. Poole. Electron spin–orbit splitting in a ingaas/inp quantum well studied by means of the weak-antilocalization and spin-zero effects in tilted magnetic fields. Semicond. Sci. Technol., 20, 2005.

Appendix A

Optical Lithography Recipe

Optical lithography recipe for InSb (Hall Bars/mesas)

A. Switch on mask aligner, let lamp warm up $>$ 30 min
B. Two solvent clean
1. Submerge in acetone, sonicate 2 min
2. IPA, sonicate 2 min
3. Blow dry with N_2 on both sides
4. Bake on a hotplate for 3 min @185° C
5. Rinse the mask with acetone and IPA directly from squeeze bottle to remove contaminants
6. Blow dry with N_2 on both sides
C. Spin resist
1. Spin 2 drops (or enough to cover the chip) of AZ1505 on @4000 RPM for 45 s ($=$ film thickness $\approx 1\ \mu m$)
2. Make sure the temperature of hotplate is down to 115°C
3. Soft bake @115°C for 45 s to evaporate excess solvent and harden resist
D. Develop
1. Use mask aligner, align with appropriate mask, hardcontact, expose for 8 s
2. Develop in AZ400K:H_2O(1:4) by moving the chip around in circular motion for 30 s to develop
3. Rinse in millipore water
4. Blow dry with N_2

Starting over
1. Sonicate in acetone for 5 min
2. Repeat from B

Appendix B

Electron Beam Lithography Recipe

A. Two solvent clean:
1. Acetone, sonicate 2 min
2. IPA, sonicate 2 min
3. Blow dry with N_2 on both sides
4. Bake on a hotplate for 3 mins @ 185°C

NB: One of the sonicators shuts off automatically after 5 min

B. Spin resist

For large features ($\approx$10 μm). Resist stack$\approx$ 480nm:
1. EL-9 (9% copolymer), 4000 rpm, 40s. Slowly rotating chip when dispensing resist.
2. Postbake, 2 mins @ 180°C
3. A4 (4% PMMA), 4000 rpm, 40s. Slowly rotating chip when dispensing resist.
4. Postbake, 2 mins @ 180°C

C. Exposure settings

I_c	Writefield	Dotmap	Dose	Dwelltime
20 nA	600 μm	20000	835 $\mu c/cm^2$	0.375 $\mu s/dot$

D. Elionix settings

These numbers, apart from aperture, are approximate and tend to wander over time.

Aperture	B_c	Focus	Stigmation
3	636	-316	-42:84

E. Develop
1. Leave in MIBK:IPA (1:3) for 90 s
2. Rinse in IPA for 5-8 s by gently rocking the chip back and forth
3. Blow dry with N_2

Appendix C

Ohmic Contacts Deposition

A. Material Deposition
Evaporate the following materials while rotating the sample holder at 30RPM.
1. 12 nm palladium (Pd)
2. 15 nm platinum (Pt)
3. 150 nm gold (Au)

B. Lift-off:
1. Two hours on hotplate in acetone @60°C
2. Sonicate 2 min
3. Rinse with IPA directly from squeeze bottle
4. Blow dry with N_2

Appendix D

Annealing

A modified recipe from Brad Boos from Naval Research Lab.

Anneal the sample for one hour at 175°C in Formier10 gas (90% N_2, 10% H2).
The process gases are Formier10 and N_2, the latter is used for venting the chamber.
Choosing the pre-programmed recipe 'marina.rcp' will take you through following steps:

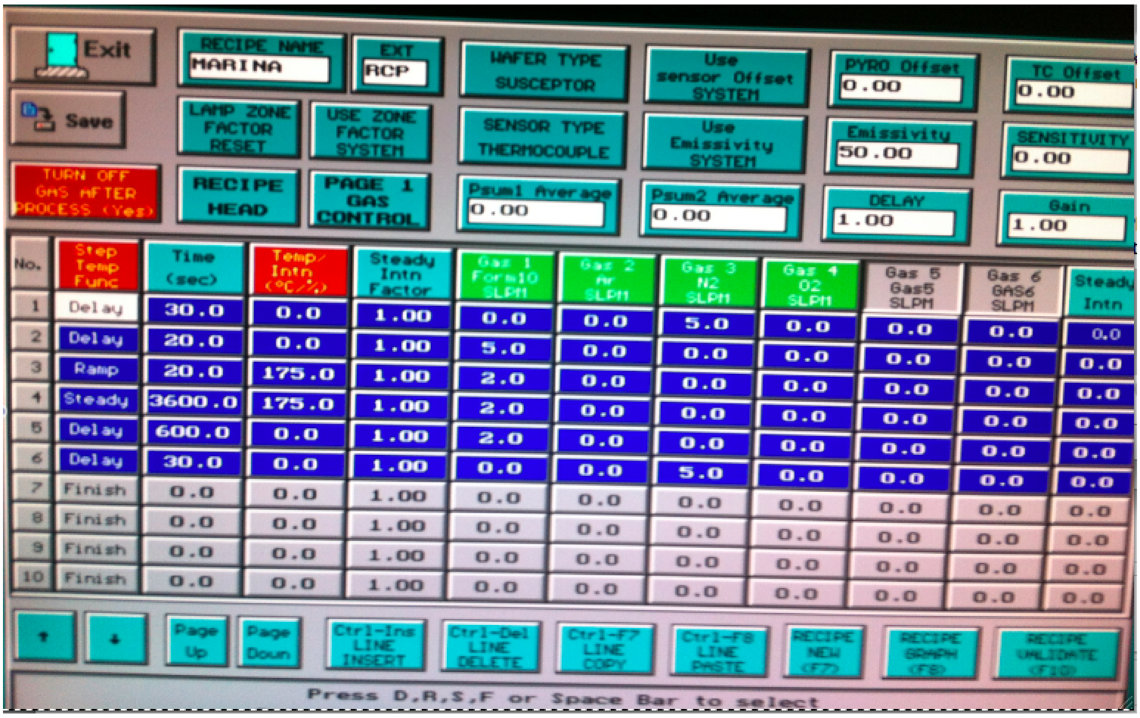

Figure D.1: *Picture of the 'marina.rcp' recipe.*

Appendix E

Extracting Values from Hall Effect Measurement

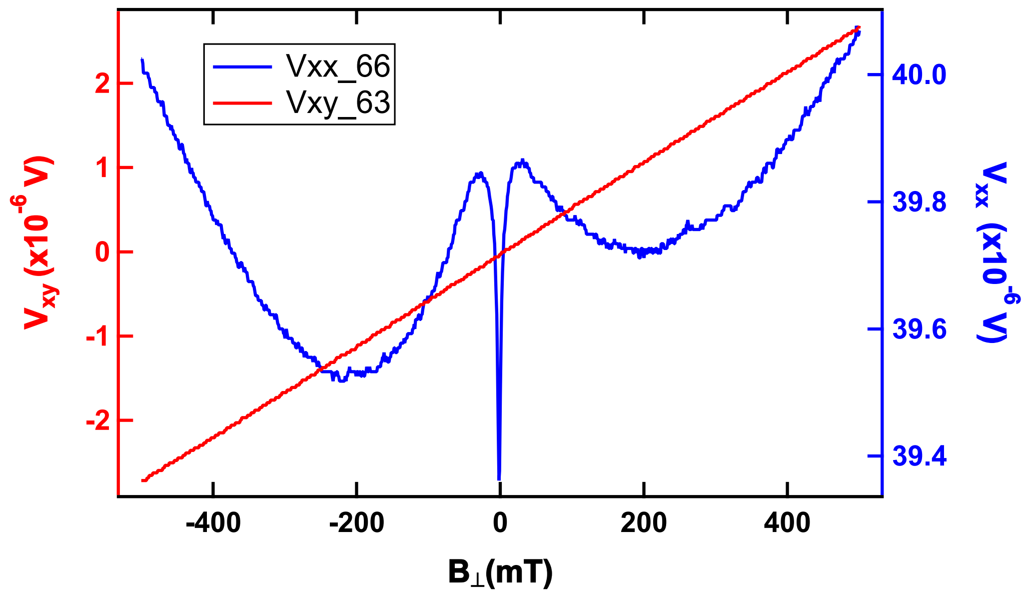

Figure E.1: *Typical Hall measurement. V_{xx} is the longitudinal voltage measurement, V_{xy} is the Hall voltage, $B_\perp$ is the perpendicular magnetic field.*

Density is calculated from the slope of the Hall voltage measurement

$$n_s = \frac{IdB}{|e|dV_{xy}} \tag{E.1}$$

where I is the current through the sample, $|e|$ is the elementary charge and dB/dV_{xy} is the gradient of the Hall voltage vs. the magnetic field, B. Conventionally presented in units of cm^{-2}.

Mobility, μ, is calculated from the longitudinal measurement:

$$\mu = \frac{I/|e|}{n_s V_{xx} W/L} \tag{E.2}$$

where V_{xx} is the longitudinal voltage and W/L is the ratio between the width of the Hall bar and distance between the voltage probes. V_{xx} is usually read out at the lowest part of the 'wing'. Conventionally presented in units of $\frac{cm^2}{Vs}$.

Sheet resistivity:

$$\rho_{xx} = \frac{V_{xx}}{I}\frac{W}{L} \tag{E.3}$$

Fermi wave vector:

$$k_F = \sqrt{2\pi n_s} \tag{E.4}$$

Fermi wavelength:

$$\lambda_F = 2\pi/k_F = \sqrt{2\pi/n_s} \tag{E.5}$$

Fermi velocity:

$$v_F = \frac{\hbar k_F}{m^*} \tag{E.6}$$

where m^* is the effective mass.
Mean free path:

$$l_e = v_F\tau_e = \frac{\rho_{xx}^{-1}h}{k_F e^2} \tag{E.7}$$

where h is Planck constant and τ_e is the momentum relaxation time.

Momentum relaxation time:

$$\tau_e = \frac{l_e}{v_F} = \frac{l_e m^*}{\hbar k_F} \tag{E.8}$$

Diffusion constant:

$$D = \frac{l_e^2}{2\tau_e} = \frac{1}{2}v_F^2\tau_e \tag{E.9}$$

Estimating the appearance of Shubnikov-de Haas oscillations:

$$B_\perp >> \mu^{-1} \tag{E.10}$$

that is, the applied perpendicular magnetic field has to be larger than the inverse of the mobility of the sample. Low mobility means larger field required to observe SdH and the other way around.

Number of occupied Landau levels (LL):

$$\#_{LL} = \frac{n_s}{2eB/h} \tag{E.11}$$